Inferring the Mass Content of Galaxy Clusters with Satellite Kinematics and Jeans Anisotropic Modeling

Rui Shi[1,2] , Wenting Wang[1,2] , Zhaozhou Li[3] , Ling Zhu[4] , Alexander Smith[5] , Shaun Cole[5] , Hongyu Gao[1,2] , Xiaokai Chen[1,2] , Qingyang Li[1,2] , and Jiaxin Han[1,2]

[1] Department of Astronomy, Shanghai Jiao Tong University, Shanghai 200240, People's Republic of China; wenting.wang@sjtu.edu.cn
[2] Shanghai Key Laboratory for Particle Physics and Cosmology, Shanghai 200240, People's Republic of China
[3] Centre for Astrophysics and Planetary Science, Racah Institute of Physics, The Hebrew University, Jerusalem, 91904, Israel
[4] Shanghai Astronomical Observatory, Chinese Academy of Sciences, 80 Nandan Road, Shanghai 200030, People's Republic of China
[5] Institute for Computational Cosmology, Department of Physics, Durham University, South Road, Durham DH1 3LE, UK

Abstract

Satellite galaxies can be used to indicate the dynamic mass of galaxy groups and clusters. In this study, we apply the axisymmetric Jeans Anisotropic Multi-Gaussian Expansion (JAM) modeling to satellite galaxies in 28 galaxy clusters selected from the TNG300-1 simulation with halo masses of $\log_{10} M_{200}/M_\odot > 14.3$. If using true bound satellites as tracers, the best constrained total mass within the half-mass radius of satellites, $M(<r_{half})$, and the virial mass, M_{200}, have average biases of -0.01 and 0.03 dex, with average scatters of 0.11 dex and 0.15 dex. If selecting companions in the redshift space with a line-of-sight depth of $2000 \, \mathrm{km \, s^{-1}}$, the biases are -0.06 and 0.01 dex, while the scatters are 0.12 and 0.18 dex for $M(<r_{half})$ and M_{200}. By comparing the best-fitting and actual density profiles, we find that $\sim 29\%$ of the best-fitting density profiles show very good agreement with the truth, $\sim 32\%$ display over/underestimates at most of the radial range with biased $M(<r_{half})$, and 39% show under/overestimates in central regions and over/underestimates in the outskirts, with good constraints on $M(<r_{half})$; yet most of the best constraints are still consistent with the true profiles within 1σ statistical uncertainties for the three circumstances. Using a mock DESI Bright Galaxy Survey catalog with the effect of fiber incompleteness, we find DESI fiber assignments and the choice of flux limits barely modify the velocity dispersion profiles and are thus unlikely to affect the dynamical modeling outcomes. Our results show that with current and future deep spectroscopic surveys, JAM can be a powerful tool to constrain the underlying density profiles of individual massive galaxy clusters.

Unified Astronomy Thesaurus concepts: Galaxy dark matter halos (1880); Galaxy clusters (584); Hydrodynamical simulations (767)

1. Introduction

Galaxy clusters in our Universe, which contribute to the most luminous end of galaxy distribution and are hosted by the most massive populations of dark matter halos, are essential objects to study (e.g., Yang et al. 2007, 2021; Rykoff et al. 2014). They provide suitable environments to examine the quenching of star formation in both the central massive galaxies and other smaller member satellite galaxies (e.g., Kimm et al. 2009; Wetzel et al. 2013; Boselli et al. 2016; Wang et al. 2018; Pintos-Castro et al. 2019), investigate the hot gas distribution through X-ray and Sunyaev–Zeldovich (SZ) observations (e.g., Arnaud et al. 2010; Planck Collaboration et al. 2013; Lim et al. 2018), study the connection between galaxies, hot gas, and the host dark matter halos (e.g., Planck Collaboration et al. 2013; Anderson et al. 2015; Wang et al. 2016), look for missing baryons (e.g., Hernández-Monteagudo et al. 2015; De Graaff et al. 2019; Lim et al. 2020), and even serve as promising standard rulers in cosmology (e.g., Wagoner et al. 2021).

In the era of precision cosmology, accurate determination of the total mass of galaxy clusters, which is dominated by invisible dark matter, is a very important prerequisite for robust scientific conclusions in these different fields. Observationally,

there are a few different approaches to constrain the mass of galaxy clusters. This includes nonkinematical methods of weak gravitational lensing (e.g., Rasia et al. 2012; Han et al. 2015; Sun et al. 2022) and modeling of the redshift distortions (e.g., Li et al. 2012). Other kinematical methods include, for example, mass estimates based on the overall line-of-sight velocity (LOSV) dispersion of member satellite galaxies through calibrations with numerical simulations (e.g., Sales et al. 2007) and through the Halo Occupation Distribution framework (e.g., More et al. 2009a, 2009b, 2011), caustic method (e.g., Diaferio & Geller 1997; Diaferio 1999; Gifford et al. 2013), dynamical modeling of the observed hot gas distribution (e.g., Rasia et al. 2012; Foëx et al. 2017), virial theorem (e.g., Biviano et al. 2006), Jeans or another more sophisticated dynamical modeling (e.g., Mamon et al. 2013; Old et al. 2014), and machine learning (e.g., Kodi Ramanah et al. 2021) approaches to recover the cluster mass from the projected phase-space distribution of satellite galaxies, and more recently, a combination of the satellite kinematics and luminosity functions under a hierarchical Bayesian inference formalism (van den Bosch et al. 2019).

Among the different satellite kinematic-based methods above, the virial mass estimator and the machine learning approach usually give a single estimate of the total cluster mass. The machine learning approach, the empirical relation deduced by Sales et al. (2007), and the modeling of redshift distortion (Li et al. 2012) often rely on external numerical simulations. Compared with the other methods, dynamical

modeling of satellite galaxies can in principle constrain a parameterized mass or potential model and does not require external simulations, but it requires a relatively large sample of satellite galaxies as dynamical tracers.

There are many deep spectroscopic surveys, such as the Sloan Digital Sky Survey V (SDSS-V; Kollmeier et al. 2017), the Subaru Prime Focus Spectroscopy (Takada et al. 2014), the Dark Energy Spectroscopic Instrument (DESI; DESI Collaboration et al. 2016; Myers et al. 2023), and future Stage-5 spectroscopic instruments such as MegaMapper (Schlegel et al. 2022) and the Maunakea Spectroscopic Explorer. For the most massive galaxy clusters in our local Universe, it is very promising to obtain the LOSVs for $> \sim 100$ member satellite galaxies, hence enabling the modeling of the parameterized mass/potential profiles, instead of only a single value of the total mass.

However, like the virial theorem, dynamical equilibrium has to be assumed for almost all dynamical modeling approaches. Since massive galaxy clusters assemble late, they may deviate more from equilibrium than less massive galaxy groups. The modeling outcome may be biased from the truth. In order to understand the amount of biases in the dynamical modeling of galaxy clusters, we first adopt realistic galaxy cluster systems from the Illustris-TNG300 simulations (Springel et al. 2018) to test the model performance with the axisymmetric Jeans Anisotropic Multi-Gaussian Expansion modeling method (JAM; Cappellari 2008; Watkins et al. 2013). In our work, we directly know the true density profiles from the simulations, and we apply JAM to the kinematics of simulated satellite galaxies, to recover the mass density profiles. In this way, we are capable of evaluating the model performances and biases, before applying the method to real data in our planned future studies. In addition to the Illustris-TNG300 simulation, we also adopt a mock DESI bright galaxy survey (BGS) catalog (Smith et al. 2017), to investigate observational effects including the fiber incompleteness and the dependence on the survey flux limit.

The layout of this paper is as follows. We introduce the TNG suites of simulations, our selections of galaxy clusters, satellite galaxies as tracers, and the creation of mock galaxy images and multi-Gaussian expansion in Section 2. Section 3 provides an introduction to the dynamical modeling method. Results are presented in Section 4, including demonstrations of the model performance based on bound satellites and satellites selected in the redshift space with contaminations. We also discuss the impact of fiber incompleteness and the effect of flux limits on our analysis. We conclude in Section 5.

2. Data

2.1. The IllustrisTNG Simulation

The sample of galaxy clusters is constructed from the TNG300-1 simulation of the IllustrisTNG Project (Pillepich et al. 2018; Springel et al. 2018). The IllustrisTNG simulations are a suite of hydrodynamical simulations incorporating sophisticated baryonic processes, carried out with a moving-mesh code (Springel 2010) to solve the equations of gravity and magnetohydrodynamics. They include comprehensive treatments of various galaxy formation and evolution processes, such as metal line cooling, star formation and evolution, chemical enrichment, and gas recycling. For more details about

TNG, we refer readers to Marinacci et al. (2018), Naiman et al. (2018), and Nelson et al. (2018, 2019).

The TNG300 suite of simulations adopts the Planck 2015 ΛCDM cosmological model with $\Omega_m = 0.3089$, $\Omega_\Lambda = 0.6911$, $\Omega_b = 0.0486$, $\sigma_8 = 0.8159$, $n_s = 0.9667$, and $h = 0.6774$ (Planck Collaboration et al. 2016). TNG300-1 is the simulation with the highest resolution in its suite (compared with TNG300-2 and TNG300-3), and hereafter we refer to it as TNG300. It has a periodic comoving box with 302.6 Mpc on each side that follows the joint evolution of 2500^3 dark matter particles and approximately 2500^3 baryonic resolution elements (gas cells and star particles). Each dark matter particle has a mass of $5.9 \times 10^7 M_\odot$, while the baryonic mass resolution is $1.1 \times 10^7 M_\odot$. Collisionless particles, such as dark matter and stars, have a softening length of 1.5 kpc, whereas gas particles have variable softening scales with a minimum of 370 pc.

2.2. Galaxy Cluster Systems in TNG

Dark matter halos in TNG are identified with the friends-of-friends (FoF) algorithm (Davis et al. 1985). In each FoF group, substructures (subhalos/galaxies) are identified with the SUBFIND algorithm (Springel et al. 2001). The most massive subhalo in each group, together with its baryonic component, is called the main subhalo and the central galaxy. All other subhalos/galaxies in the halo are referred to as satellites.

In our study, we first select massive galaxy clusters with $M_{200} > 10^{14.3} M_\odot$ [6] from the redshift zero snapshot of TNG300. There are 86 galaxy clusters falling within this mass range in TNG300. Most of these massive clusters with $M_{200} > 10^{14.3} M_\odot$ can have more than 100 bound satellites[7] with a stellar mass threshold of $M_\odot > 10^9 M_\odot$ [8] and projected within 2 Mpc. At the lower boundary of $M_{200} \sim 10^{14.3} M_\odot$, the minimal number of bound satellites is ~ 70. The number of satellites is enough for dynamical modeling. We further select cluster systems by requiring the central galaxies of these clusters to be at least two magnitudes brighter in the r band than the brightest companions projected within 4 Mpc and with LOSV differences with respect to the central galaxies smaller than 2000 km s^{-1}. These selections result in 28 clusters that meet these requirements.

In Figure 1, we show the distribution of the number of bound satellites and M_{200} for these galaxy clusters. In particular, we show in the right panel of Figure 1 the distribution of middle-to-major axis ratios (b/a) for our selected galaxy cluster systems (black) and all galaxy clusters with the same mass threshold of $M_{200} > 10^{14.3} M_\odot$ in TNG300. Here b/a is calculated by using all bound star particles within R_{200} in these cluster systems, including those in bound satellite galaxies. Our selected clusters have $b/a > 0.45$.

We choose the Z-axis[9] of the TNG300 simulation box as the line-of-sight direction. We define, for the observing frame, the

---

[6] The virial mass, M_{200}, is defined as the mass enclosed in a radius, R_{200}, within which the mean matter density is 200 times the critical density of the universe.

[7] Bound satellites are defined as those companion galaxies around each galaxy cluster system that have total energy smaller than zero in the simulation.

[8] This mass threshold is chosen to ensure that the satellites can have more than ~ 100 star particles in TNG300.

[9] In this paper, we will have three different coordinate systems. The first one is the X-, Y-, and Z-axes of the simulation box, which we denote using capital letters. The observing frame is defined using letters with a prime symbol, i.e., x', y', and z'. In Section 3.1 below, we will define another intrinsic coordinate system centered on the central galaxy, which we denote using x, y, and z.
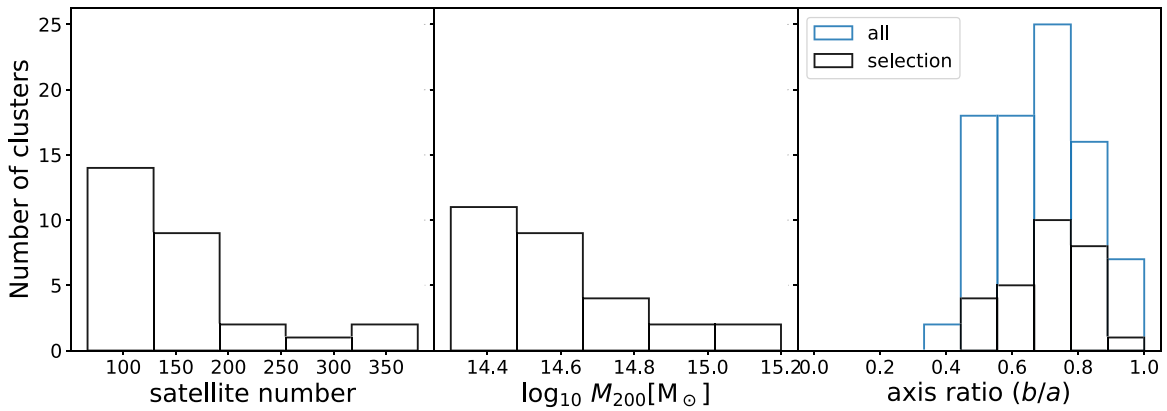
Figure 1. Distribution of the number of bound satellites in each cluster (left), the virial mass (M_{200}, middle), and the middle-to-major axis ratio (b/a, right) for our mock galaxy clusters from TNG300. In the right panel, the black and blue histograms refer to our selected galaxy clusters and all clusters with the same halo mass threshold in TNG300, respectively.

z'-axis as aligned with the line-of-sight direction, and the $x' - y'$ plane to be perpendicular to the line-of-sight direction. Here the x'-axis is defined as the image major axis of the galaxy cluster in projection. Notably, the observing frame is a left-handed system.

The central coordinate of each galaxy cluster is defined as the potential minimum of the main subhalo, and the velocity of each cluster is defined as the mass-weighted and averaged velocity based on all particles in the main subhalo. The velocity of each satellite is calculated relative to the velocity of the cluster after considering the Hubble flow. Explicitly, the LOSVs of satellites in galaxy clusters from TNG300 are calculated as $v_{los} = H_0(Z - Z_{cen}) + (v_Z - v_{Z,cen})$. Here Z_{cen} and $v_{Z,cen}$ are the Z coordinate and the velocity along the Z-axis of the simulation box for the cluster center, while Z and v_Z are the corresponding coordinate and velocity for the satellite. H_0 is the Hubble constant at redshift zero.

For results based on TNG300 in this study, we select dynamical tracer satellite galaxies in two different ways. We first select only true bound satellite galaxies projected within 2 Mpc and more massive than $10^9 M_{\odot}$ as dynamical tracers. Then, to mimic real observation, satellites are selected as those projected within 2 Mpc, within 2000 km s^{-1} along the line-of-sight direction, and also more massive than $10^9 M_{\odot}$. Our choice of the line-of-sight depth is based on a natural boundary of dark matter halos revealed around the minimum bias and maximum infall locations, and this boundary is very close to twice the virial radius of dark matter halos, which is close to 2000 km s^{-1} along the line of sight for our massive galaxy cluster systems (e.g., Fong & Han 2021; Fong et al. 2022; Gao et al. 2023). We find the completeness of satellites selected in this way is ∼88% on average, and the contamination is ∼11%. In our analysis, we will test how the dynamical modeling outcome changes with the contamination.

2.3. The DESI BGS Mock Catalog

In addition to TNG galaxy cluster systems, we use a mock DESI BGS catalog (Smith et al. 2017) to investigate observational effects including fiber incompleteness and flux limits. The DESI BGS survey is expected to cover an area of ∼14,000 square degrees in four passes of the sky, with a depth approximately two magnitudes deeper than that of the SDSS,

hence providing more spectroscopically observed satellite galaxies in galaxy clusters (Hahn et al. 2023).

The BGS mock catalog we adopted in this study is based on the Millennium-XXL (MXXL) simulation (Angulo et al. 2012), which adopts the WMAP1 cosmological parameters of $\Omega_m = 0.25$, $\Omega_\Lambda = 0.75$, $\sigma_8 = 0.9$, $n = 1$, and $h = 0.73$. It is a light-cone mock catalog (Smith et al. 2017), which covers the full sky and extends to redshift 0.8 with a mass resolution of $\sim 10^{11.14} M_{\odot}$. The light cone is created with interpolation between different snapshots (Merson et al. 2013).

Satellites are randomly positioned following a Navarro–Frenk–White (Navarro et al. 1996, 1997) density profile, with randomly assigned velocities following the Maxwell–Boltzmann distribution. A Monte Carlo method is used to assign an r-band magnitude and a $g - r$ color to each galaxy to build a galaxy catalog whose luminosity function of galaxies is in agreement with the SDSS (Abazajian et al. 2009) and the Galaxy and Mass Assembly survey (Driver et al. 2009, 2011). The galaxy catalog has a flux limit of $r < 20$ and a median redshift of $z \sim 0.2$. The flux limit of $r < 20$ is faint enough for the DESI BGS bright sample, as the BGS bright sample has a flux limit of $r < 19.5$. The fiber assignment algorithm has been run on the mock (Smith et al. 2019), enabling us to quantify the impact of fiber assignment in galaxy surveys.

Note, however, that the fiber assignment algorithm of Smith et al. (2019) is currently being updated with the progress of the DESI observation. The mock BGS catalog we are currently using in this study (Smith et al. 2017) is based on three passes, and it is now being updated to four passes. Moreover, the DESI BGS survey has a faint sample down to a flux limit of $r < 20.175$, in order to increase the overall BGS target density and enable small-scale clustering measurements (Hahn et al. 2023). Thus the flux limit is being updated from $r < 20$ to $r < 20.175$ in the latest DESI BGC mock under construction. Nevertheless, we think these improvements and modifications will not affect our conclusions (see Section 4.5 for details).

We select tracer satellites from the DESI BGS mock as those companions that are projected within R_{200} and with LOSV differences with respect to the central galaxy smaller than twice the virial velocity of the host halos. After applying DESI masks, we find that there are 84 galaxy clusters with redshifts lower than 0.2 within the DESI Year 5 footprint, which can have more than 100 satellite galaxies with $r < 19.5$ selected in this way. The LOSVs (v_{los}) of the satellite galaxies in the BGS
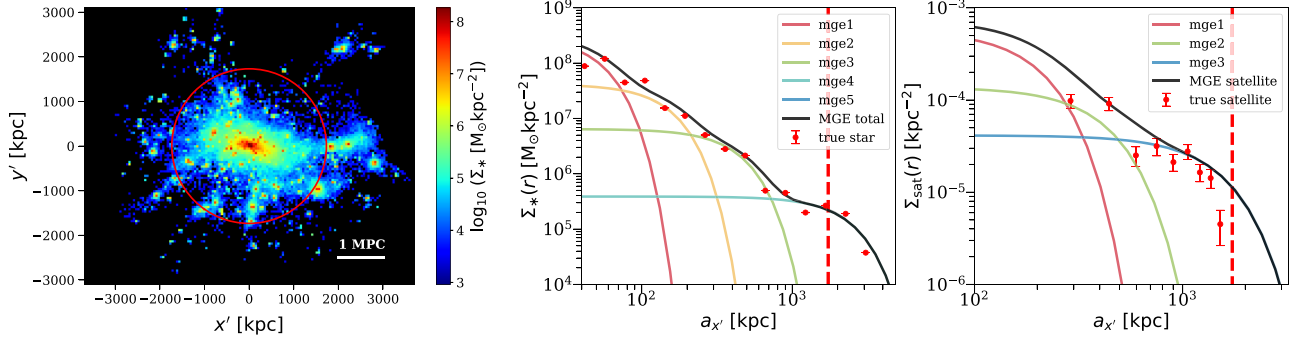
Figure 2. Left: surface density map for the stellar component of one representative galaxy cluster system from TNG300. The red circle corresponds to R_{200}. Middle: the red dots with error bars are the true surface density profile of the total stellar mass distribution. This is calculated from elliptical isophotes and reported as a function of the major axis length ($a_{x'}$) for the same representative galaxy cluster in the left plot. The error bars are the 1σ scatters based on 100 bootstrap samples of all star particles in TNG300, which are comparable to the symbol size. We show each individual MGE component with a different colored curve, and the black solid curve is the total best-fitting surface density profile, contributed by the combination of all MGEs. The red vertical dashed line marks R_{200}. Right: similar to the left panel, but comparing the true projected satellite number density profile and the MGE decompositions. The error bars are the 1σ scatters among 100 bootstrap satellite samples.

mock catalog are calculated based on the following equation:

$$v_{\rm los} = \frac{c({\rm redshift} - {\rm redshift}_{\rm cen})}{1 + {\rm redshift}_{\rm cen}}, \qquad (1)$$

where c is the speed of light, ${\rm redshift} - {\rm redshift}_{\rm cen}$ is the difference between the redshifts of the satellite galaxy and the central galaxy of the galaxy cluster.

The mock DESI BGS catalog is based on different cosmological parameters from those of TNG, with satellites populated in dark matter halos in different ways. In principle, it is better to focus on the same simulation, but TNG does not have realistic light-cone mocks. We thus checked the average distribution of the LOSV, velocity dispersion, and surface number density profiles of satellite galaxies in the two simulated data sets (TNG and DESI BGS catalog), and we found consistent spatial and velocity distributions of satellites, which ensures a fair usage of the mock DESI BGS catalog.

2.4. Mock Galaxy Cluster Images and Multi-Gaussian Decomposition

In our study, we aim to constrain the underlying potential using satellite galaxies as dynamical tracers. The potential is contributed by both luminous and dark matter. JAM directly infers the potential formed by the luminous matter distribution from the deprojected "optical" image. Hence we need to create mock galaxy cluster images for our analysis. For the mock images of galaxy clusters, we simply adopt the projected stellar mass density or surface density to create the images, i.e., the reading in each pixel is in units of $M_\odot\,{\rm pc}^{-2}$ based on all bound star particles associated with the galaxy cluster. Note the mock images of galaxy clusters are contributed by all star particles bound to the cluster and also those star particles in satellite galaxies bound to the cluster. In real observations, however, the observed diffuse light in the outskirts of the clusters depends on the surface brightness limit of the optical survey but can be well measured for individual galaxy clusters in modern deep photometric surveys (e.g., Huang et al. 2018; Wang et al. 2019).

The projected number density distribution of tracer satellites plays a critical role in solving the Jeans equation (see Section 3.1 for more details). Therefore, we also create the projected satellite number density maps for each galaxy cluster

system, based on the projected positions of selected tracer satellite galaxies, with each satellite contributing the same weight, regardless of its actual stellar mass or luminosity in the simulation.

Once the mock images or maps are made, the projected luminous stellar mass distributions and the projected satellite number distributions will be decomposed to multiple Gaussian elements (MGEs; Emsellem et al. 1994; D'Souza & Rix 2013), in order to enable the analytical deprojection for each MGE component to three dimensions and to bring analytical solutions for any arbitrary matter distribution (see Section 3 for more details).

In practice, we execute the MGE decomposition with the Sherpa software (Freeman et al. 2001; Doe et al. 2007), which is a modeling and fitting module integrated with CIAO to fit the mock images and optimize the solutions of each MGE.

The surface density distribution is shown for one example galaxy cluster from TNG300 in the left plot of Figure 2. Note JAM requires the major axes of the mock galaxy and tracer images to align with the x'-axis of the image plane, and thus the galaxy cluster has been rotated to meet the requirement.

In the middle panel, we show each individual Gaussian element of the stellar component with different colored curves for this cluster. The combined surface density profile of all MGEs is represented by the black curve, and the true surface density profile of the stellar component is shown by red dots. From this plot, we can see the red dots agree well with the black line from $\sim$100 kpc to R_{200}, indicating a good overall performance of the MGE decomposition. In the innermost region ($<$100 kpc), the black line tends to be slightly higher than the red dots, and such a bias is primarily caused by the lower number of pixels in such central regions. The right panel of Figure 2 is similar to the left one, but it shows the MGE decomposition for the projected satellite/tracer number density profile. The error bars of the red dots are based on 100 bootstrap samples of satellites in projection. In detail, we perform multiple bootstrap samples by randomly selecting a subset of these satellites each time with repeats and calculating the 1σ scatters of the projected satellite number density profiles. Because of the limited number of satellites, the error bars are significantly larger in the right plot, and the MGE decomposition is not as good as in the middle panel, especially in the very inner region and the outer region close to R_{200}.

3. Methodology

3.1. The Jeans Equation and Potential Model

JAM modeling is a powerful dynamical modeling tool that can be used to constrain the luminous and dark matter distributions of globular clusters, dwarf galaxies, and distant galaxies with integral field unit observations. In this study, we investigate the performance of JAM when it is applied to galaxy clusters, with satellite galaxies in the cluster as dynamical tracers. A detailed description of JAM can be found in Cappellari (2008) and Watkins et al. (2013). Here we only give a brief introduction.

The Jeans equation for an axisymmetric system ($\frac{\partial}{\partial \phi} = 0$) in steady state ($\frac{\partial}{\partial t} = 0$) can be written in cylindrical coordinates as

$$\frac{\nu(\overline{v_R^2} - \overline{v_\phi^2})}{R} + \frac{\partial(\nu\overline{v_R^2})}{\partial R} + \frac{\partial(\nu\overline{v_R v_z})}{\partial z} = -\nu\frac{\partial\Phi_{\text{tot}}}{\partial R}, \qquad (2)$$

$$\frac{\nu\overline{v_R v_z}}{R} + \frac{\partial(\nu\overline{v_R v_z})}{\partial R} + \frac{\partial(\nu\overline{v_z^2})}{\partial z} = -\nu\frac{\partial\Phi_{\text{tot}}}{\partial z}, \qquad (3)$$

where ν is the satellite number density distribution, which has been decomposed into a few different MGEs (see Section 2.4 for details). Φ_{tot} is the total gravitational potential.

JAM models the total potential, Φ_{tot}, with two different components: (1) the stellar component, as we have mentioned in Section 2.4, which is deprojected and evaluated from the surface density distribution;[10] and (2) the dark matter component.[11] To model the dark matter component, we simply adopt the following the double-power-law model:

$$\rho(r) = \frac{\rho_s}{(r/r_s)^\gamma(1 + r/r_s)^\alpha}, \qquad (4)$$

in which ρ_s and r_s are the scale density and scale radius, and α is the outer power law index. In this study, due to the significantly lower number of satellite galaxies in central regions of the galaxy clusters, we find that our constraints on the inner density slope, γ, are very weak, so we fix γ to be 1 throughout this paper.

As we have mentioned in Section 2.4, JAM determines the potential contributed by the stellar mass distribution from the deprojected optical images of galaxy clusters. Since the pixel units of our mock images are $M_\odot \, \text{pc}^{-2}$, we simply fix the stellar-mass-to-light ratio (M_*/L) to unity in our analysis. We decompose the stellar mass distribution into MGEs. Each component enables fast deprojections and leads to quick analytical solutions to the Jeans equation. Given a model dark matter density profile, we also decompose it into a few different MGEs (see Section 2.4 for details). In this way, we have MGE

components for the luminous and dark matter potential, and tracer number density distribution, ν. We can thus have analytical solutions for each MGE component. The final solution to the above Jeans equation (Equations (2) and (3)) is the summation of all different components.

To ensure that the Jeans equation has unique solutions of the first and second velocity moments, the velocity ellipsoid is further assumed to be aligned with the cylindrical polar coordinate system ($\overline{v_R v_z} = 0$). In addition, a constant anisotropy parameter, λ, is introduced as $\overline{v_R^2} = \lambda\overline{v_z^2}$. A rotation parameter, κ, is introduced as $\overline{v_\phi} = \kappa(\overline{v_\phi^2} - \overline{v_R^2})^{1/2}$, with the calculation of it modified according to Zhu et al. (2016), though for galaxy clusters, which are not rotation-dominated systems, κ is not expected to be significantly different from zero. In principle, κ can be either positive or negative, depending on the direction of rotation, i.e., clockwise or counterclockwise seeing from the positive z-axis in the intrinsic frame (see the definition below for the intrinsic frame). With the boundary condition set to $\nu\overline{v_z^2} = 0$ as $z \to \infty$, the Jeans equation can be summarized as

$$\nu\overline{v_\phi^2}(R, z) = \lambda\left[R\frac{\partial(\nu\overline{v_R^2})}{\partial R} + \nu\overline{v_z^2}\right] + R\nu\frac{\partial\Phi}{\partial R}, \qquad (5)$$

$$\nu\overline{v_z^2}(R, z) = \int_z^\infty \nu\frac{\partial\Phi}{\partial z}dz. \qquad (6)$$

Given a model potential, the velocity first and second moments are solved in an intrinsic frame defined on the cluster system. The intrinsic frame is a right-handed system, and we use the quantities without the prime to denote the intrinsic frame, i.e., x, y, and z. In our analysis, the z-axis is chosen to be the minor axis of the cluster system, with the minor axis calculated from the spatial distribution of satellites. The x-axis is chosen to be aligned with the x'-axis of the observing frame (see Section 2.2 above), with the x'-axis being the projected major axis of the galaxy cluster in the image plane. The y-axis is determined according to the x-axis and z-axis to form the right-handed cartesian coordinate system. The intrinsic frame can be linked to the left-handed observing frame (see Section 2.2) through the following equations:

$$\begin{pmatrix} x' \\ y' \\ z' \end{pmatrix} = \begin{pmatrix} 1 & 0 & 0 \\ 0 & -\cos(incl) & \sin(incl) \\ 0 & \sin(incl) & \cos(incl) \end{pmatrix}\begin{pmatrix} x \\ y \\ z \end{pmatrix}, \qquad (7)$$

where *incl* is the inclination angle, defined as the angle between the z-axis of the intrinsic frame and the z'-axis of the observing frame.

The first and second moments of LOSVs, solved from the Jeans equation mentioned above, can be compared with the actual velocity moments of tracer satellites. Then the best potential model parameters can be inferred by maximizing the likelihood function, which will be introduced in the next section.

---

[10] The stellar component is subdominant compared with dark matter in galaxy clusters, and throughout this paper, we focus our discussions on the constraints of the total matter distribution.

[11] JAM does not model the gas component separately, because in real observation, the spatial distribution of hot and cold gas in distant galaxies is often difficult to be directly observed with high resolution. In principle, we can modify JAM to model the gas component separately. However, we have checked that the hot gas component is distributed over the whole halo and has similar radial distributions as that of dark matter. Even if we model the gas and dark matter components separately, JAM would fail to distinguish them. So for our analysis throughout this paper, the gas component would be modeled within the dark matter component. Since our main conclusions are based on the total matter distribution, whether the gas component is modeled separately or not is not important.

3.2. Likelihood Function

We model the posterior probability distribution of our model parameters by Bayes theorem:

$$p(\boldsymbol{\Theta}|\boldsymbol{D}) = \frac{p(\boldsymbol{D}|\boldsymbol{\Theta})p(\boldsymbol{\Theta})}{p(\boldsymbol{D})}. \tag{8}$$

Our list of model parameters is $\boldsymbol{\Theta} = (\lambda, \kappa, \rho_s, r_s, \alpha)$ (see Section 3.1 above or a summary of free parameters near the end of this subsection). $p(\boldsymbol{\Theta})$ is the prior, and $p(\boldsymbol{D}|\boldsymbol{\Theta})$ is the distribution of the velocities by assuming that the prediction of the velocity distribution obeys the multivariate Gaussian distribution. $p(\boldsymbol{D})$ is a factor required to normalize the posterior.

The likelihood of the satellites in each cluster system can be written as

$$
\begin{aligned}
L_{\text{tot}}^{\text{sat}} &= p(\boldsymbol{D}|\boldsymbol{\Theta}) \\
&= \prod_{i=1}^{N_{\text{sat}}} p(\boldsymbol{v}_i|\boldsymbol{x}_i', \boldsymbol{S}_i, \boldsymbol{\Theta}) \\
&= \prod_{i=1}^{N_{\text{sat}}} \frac{\exp\left[-\frac{1}{2}(\boldsymbol{v}_i - \boldsymbol{\mu}_i)^{\text{T}}(\boldsymbol{C}_i + \boldsymbol{S}_i)^{-1}(\boldsymbol{v}_i - \boldsymbol{\mu}_i)\right]}{\sqrt{(2\pi)^3|(\boldsymbol{C}_i + \boldsymbol{S}_i)|}},
\end{aligned} \tag{9}
$$

where $\boldsymbol{v}_i$ represents the velocity solved by JAM at the position of the observed tracer satellite, $\boldsymbol{x}_i' = (x_i', y_i')$, and $\boldsymbol{\mu}_i$ is the observed velocity of the tracer satellite.

The covariance matrix $\boldsymbol{C}_i$ is defined through the first and second velocity moments:

$$
\boldsymbol{C}_i =
\begin{pmatrix}
\overline{v_{x',i}^2} - \overline{v_{x',i}}^2 & \overline{v_{x'y',i}^2} - \overline{v_{x',i}}\,\overline{v_{y',i}} & \overline{v_{x'z',i}^2} - \overline{v_{x',i}}\,\overline{v_{z',i}} \\
\overline{v_{x'y',i}^2} - \overline{v_{x',i}}\,\overline{v_{y',i}} & \overline{v_{y',i}^2} - \overline{v_{y',i}}^2 & \overline{v_{y'z',i}^2} - \overline{v_{y',i}}\,\overline{v_{z',i}} \\
\overline{v_{x'z',i}^2} - \overline{v_{x',i}}\,\overline{v_{z',i}} & \overline{v_{y'z',i}^2} - \overline{v_{y',i}}\,\overline{v_{z',i}} & \overline{v_{z',i}^2} - \overline{v_{z',i}}^2
\end{pmatrix}, \tag{10}
$$

and $\boldsymbol{S}_i$ is the error matrix of the observed velocity of a tracer satellite

$$
\boldsymbol{S}_i =
\begin{pmatrix}
\sigma_{v_{x'},i}^2 & 0 & 0 \\
0 & \sigma_{v_{y'},i}^2 & 0 \\
0 & 0 & \sigma_{v_{z'},i}^2
\end{pmatrix}. \tag{11}
$$

Notably, in our work, we only use the LOSVs, so we simply set $v_{x',i} = v_{y',i} = 0$ and input very large values for $\sigma_{v_{y'},i}^2$ and $\sigma_{v_{z'},i}^2$. This is equivalent to only fitting the observed first and second moments of LOSVs.

$$m_i(\boldsymbol{x}_i') = \frac{\Sigma(\boldsymbol{x}_i')}{\Sigma(\boldsymbol{x}_i') + \epsilon\,\Sigma(0, 0)}, \tag{12}$$

where $\Sigma(\boldsymbol{x}_i')$ is the surface density at $\boldsymbol{x}_i'$ and $\Sigma(0, 0)$ is the central surface density.

The likelihood of the fore/background satellites, L_i^{bkgd}, can be calculated by assuming a tri-variate Gaussian distribution with a given mean velocity and velocity dispersion of a fore/background model. In our case, the mean velocity and velocity dispersion of the fore/background model are directly calculated from unbound satellite galaxies in the simulation. Then

the likelihood becomes

$$L = \prod_{i=1}^{N_{\text{sat}}} m_i(\boldsymbol{x}_i')L_i^{\text{sat}} + [1 - m_i(\boldsymbol{x}_i')]L_i^{\text{bkgd}}. \tag{13}$$

We summarize the list of our model parameters as follows:

1. λ, the velocity anisotropy;
2. κ, the rotation parameter;
3. $d_1 \equiv \log_{10}(\rho_s^2 r_s^3)$;
4. $d_2 \equiv \log_{10}(\rho_s)$;
5. α, the outer density slope;
6. ϵ, the background fraction;
7. $incl$, the inclination angle.

Here d_1 and d_2 are constructed to reduce the strong degeneracy between ρ_s and r_s. The logarithmic transformation converts the original units of $M_\odot^2\,\text{pc}^{-3}$ and $M_\odot\,\text{pc}^{-3}$ into dimensionless logarithmic values. After taking the logarithm, they cover a smaller range in the log space. ϵ is fixed to zero when we only consider bound satellites as tracers. To obtain the best-fitting model parameters, we set a flat prior of $\boldsymbol{\Theta}$ and use the Markov chain Monte Carlo approach[12] to maximize the likelihood function.

In our analysis, we will try two different cases by either fixing $incl$ or allowing it to be a free model parameter. When fixing $incl$, its value is chosen as the angle between the line-of-sight direction of the mock observer and the minor axis calculated from the spatial distribution of bound satellites. However, since our galaxy cluster systems are not rotationally dominated and the minor axes of realistic galaxy cluster systems differ for different components, the definition of $incl$ is not straightforward. For example, if we calculate the minor axis according to the spatial distribution of the central galaxy, the angle between this minor axis and the line-of-sight direction would be different. For individual systems, fixing $incl$ according to different minor axes definitions or treating $incl$ as a free parameter can lead to different constraints, though for most of the time, they are still consistent within 1σ due to our small number of tracer satellites. For all 28 cluster systems, we will show later that the amounts of overall biases and scatters of either fixing $incl$ or treating it as a free parameter do not show significant differences. Setting $incl$ as a free parameter leads to slightly smaller scatters. Note in real observation, the constraint on $incl$ for galaxy cluster systems is weak and $incl$ is chosen to be fixed (e.g., Li et al. 2020).

We fix the stellar-mass-to-light ratio, M_*/L, to their true values in the simulation. In our analysis, the true value of M_*/L is unity. We do not test the uncertainties in M_*/L in this study. In real observations, M_*/L can be determined through stellar population synthesis modeling and fixed upon dynamical modeling. The uncertainties of M_*/L by population synthesis modeling, however, depend on many different factors, including the number of available bands adopted for the synthesis modeling, the adopted stellar libraries, initial mass functions, dust models, and so on (e.g., Conroy 2013), which might have significant systematic uncertainties but these are hard to be directly tested for real galaxies.

Nevertheless, we find the stellar component is more subdominant than the dark matter component for our galaxy

---

[12] When fitting the double-power-law function to the true density profiles, we use EMCEE (Foreman-Mackey et al. 2013) to sample the posterior distribution of parameters.
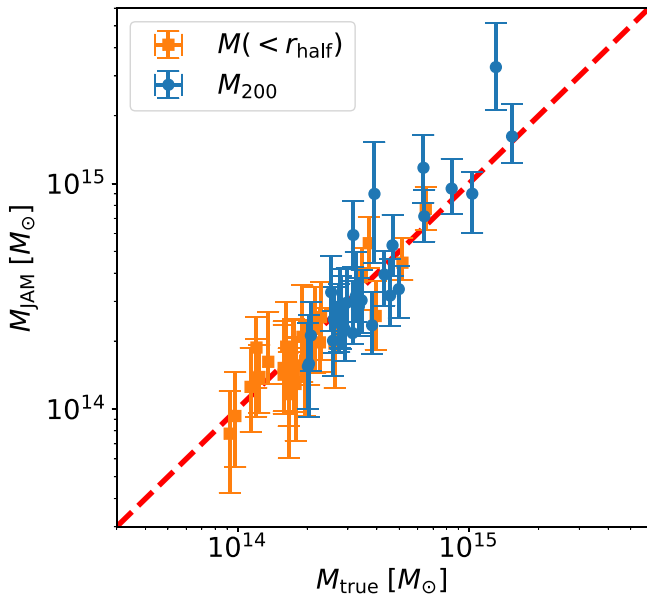
Figure 3. The blue dots with error bars show the best-fitting M_{200} by JAM vs. the true masses for 28 galaxy clusters from TNG300. Here we adopt true bound satellites as tracers, and the inclination, *incl*, is fixed to the angle between the line-of-sight direction of the mock observer and the minor axes defined through the spatial distribution of bound satellite galaxies in the simulation. The orange squares represent the best-fitting vs. true mass within the half-mass–radius of tracer satellites, $M(<r_{\mathrm{half}})$. The red dashed diagonal line marks "$y = x$" to guide the eye. Overall, JAM gives a reasonable prediction of both M_{200} and $M(<r_{\mathrm{half}})$. The error bars are calculated from the boundaries defined by those models whose log-likelihood ratios are within 1σ to the log-likelihood value of the best model, assuming χ^2 distribution for the twice log-likelihood variable.

cluster systems from TNG. Moreover, throughout our analysis in this paper, we focus on discussing the total mass profiles, so we believe uncertainties in M_*/L would not significantly affect the generality of the main conclusions about the total mass profile in this paper. In fact, in a previous study, Wang et al. (2022) found that if M_*/L is fixed to a significantly high value, JAM would decrease the contribution by dark matter, which maintains almost the same best-constrained total matter distribution. In principle, we can modify JAM to let it directly model the total matter distribution for our sample of galaxy clusters, instead of modeling the stellar and dark matter components separately, but this is not incorporated for our analysis in this current paper.

4. Results

In this subsection, we investigate the accuracy and bias of the mass profiles predicted by JAM.

4.1. The Overall Performance with Massive Galaxy Clusters from TNG300

Figure 3 shows the JAM-predicted masses versus the truth in the simulation, for all 28 galaxy clusters selected from TNG300. Here the results are based on the case when the inclination angle, *incl*, is fixed. We will discuss the case when *incl* is a free parameter later in Section 4.3. We show the comparisons between the best-fitting and the truth for the total mass enclosed within the half-mass radius of tracer satellites, r_{half}, and for the virial mass, M_{200}. Here r_{half} is defined as the projected radius, within which it contains half of the total bound tracer satellites projected within 2 Mpc. We denote the masses enclosed within r_{half} as $M(<r_{\mathrm{half}})$. Note the enclosed

Table 1
Summary of Biases and Scatters in $M(<r_{\mathrm{half}})$ and M_{200}

	Mass Bias		Mass Scatter	
	$M(<r_{\mathrm{half}})$	M_{200}	$M(<r_{\mathrm{half}})$	M_{200}
bound satellite *incl* fixed	−0.02	0.01	0.09	0.15
bound satellite *incl* free	−0.01	0.03	0.11	0.15
with contamination *incl* free	−0.06	0.01	0.12	0.18

Note. Throughout this paper, we first investigated the case when only bound satellites are used as tracers, with fixed *incl* (Section 4.1). We then moved on with the case of treating *incl* as a free model parameter, but still using bound satellites as tracers (Section 4.3). In the end, we select satellite galaxies in the redshift space as tracers, with free *incl* (Section 4.4). The three cases refer to the three rows of the table (see the text in the left column).

masses are defined in three dimensions rather than in projection, according to the best-fitting potential model and the actual particle distributions in the original simulations. The best-fitting virial mass is calculated according to the best-fitting model density profile by JAM. We first calculate the corresponding R_{200} according to the best-fitting profile and then calculate the integrated mass within R_{200}.

In general, the orange squares and the blue dots roughly distribute symmetrically around the red diagonal line, indicating reasonable and approximately ensemble unbiased mass constraints. There are small biases of −0.02 and 0.01 for $M(<r_{\mathrm{half}})$ and M_{200}. The mean scatters are ∼0.09 dex for $M(<r_{\mathrm{half}})$ and 0.15 dex for M_{200}. The readers can refer to the top row of Table 1 for a summary of these values.

According to the amounts of scatter, we can see the constraint on $M(<r_{\mathrm{half}})$ is better than that of M_{200}. This is consistent with the argument in many previous studies, which find that the mass within the half-mass radius of tracers is a sweet point, which can be constrained better than the masses within other radii (e.g., Wolf et al. 2010; Walker & Peñarrubia 2011; Wang et al. 2015; González-Samaniego et al. 2017; Wang et al. 2020). This is mainly due to the degeneracy between the two halo parameters (d_1 and d_2, ρ_s and r_s, or M_{200} and the concentration c_{200}). Perpendicular to the degeneracy direction, the constraint is the tightest, which corresponds to the amplitude of the potential at approximately the median radius of the tracer population. On the other hand, the constraint is the weakest along the degeneracy direction, which corresponds to the shape of the potential (e.g., Han et al. 2016; Li et al. 2021, 2022).

Figure 4 shows the error contours of different combinations of five model parameters (λ, κ, d_1, d_2, α) for one randomly selected galaxy cluster. The black, dark gray, and gray regions show the 1, 2, and 3σ confidence intervals. As we have mentioned above, d_1 and d_2 are defined from the two halo parameters as $d_1 \equiv \log_{10}(\rho_s^2 r_s^3)$ and $d_2 \equiv \log_{10}(\rho_s)$, and thus they are dimensionless and cover a much smaller range in the log space than the original ρ_s and r_s. The units we adopt for ρ_s and r_s are $M_\odot \, \mathrm{pc}^{-3}$ and parsec in our calculations, and d_2 can be negative. The degeneracies between d_1, d_2, and α are prominent. The degeneracies between the rotation parameter, κ, and halo parameters (d_1, d_2, and α) are very weak or absent, while there also exist some correlations between λ and the three

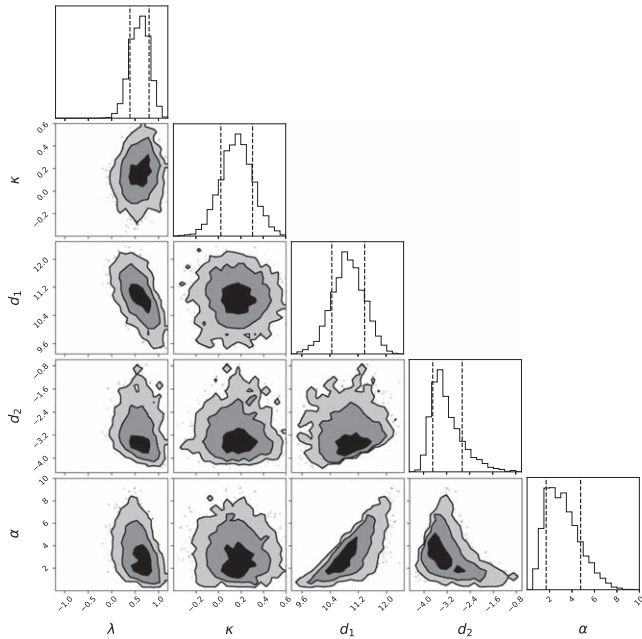**Figure 4.** Error contours for one randomly selected galaxy cluster from TNG300. The black, dark gray, and gray contours are 1σ, 2σ, and 3σ confidence levels, respectively. The histograms on the right of each row show the one-dimensional marginalized posterior distributions. The x- and y-axis ranges displayed here are chosen to be the same as in Figure 8 below.

halo parameters, though not as strong as those among the halo parameters. Note that for this galaxy cluster, κ is positive but still close to zero, indicating weak rotations. For most of our galaxy clusters, the values of κ are close to but not exactly zero, indicating galaxy clusters can have weak rotations, but they are not rotationally dominated systems. In the next subsection, we move on to investigate a few example density profiles and perform more detailed discussions.

4.2. Example Density and Velocity Dispersion Profiles

In this subsection, we further compare the best-fitting and true density and velocity dispersion profiles. Figure 5 shows the true and best-fitting matter density profiles for the dark matter + gas (orange) components and for the total matter distribution (blue). This is shown for three representative galaxy clusters. At most of the radii, the blue crosses and solid curves are very close to the orange dots and dotted curves, except for the very inner regions, which is due to the contribution of the stellar component. Note again in our JAM modeling, the gas component is not modeled separately. Instead, the hot gas is largely included in the dark matter component of the model, because they have similar distributions as the underlying dark matter in the simulation. In our analysis, the stellar component is directly deprojected from the stellar surface density distribution and is subdominant, and hence are not shown in Figure 5.

In the left panel of Figure 5, the difference between the blue crosses and the blue solid line is significantly smaller than the shaded errors, indicating the total density profile is very well recovered over the whole radial range. As we have explicitly checked, 8 out of the 28 systems ($\sim$29%) in our galaxy sample belong to this case, i.e., the density profiles are very well constrained at almost all radii within R_{200}.

In the middle panel, the best-fitting total profile more prominently deviates from the true total density profile at most of the radial range, and the total mass within the half-mass radius of tracer satellites, $M(<r_{half})$, is less well recovered. Though given the large statistical errors, the best-constrained model and the truth still marginally agree with each other. About nine galaxy clusters ($\sim$32%) show similar trends as this middle panel, among which five show overestimates over most of the radial range, and four show underestimates over most of the radial range.

In the right panel of Figure 5, the best-constrained total mass density profile is underestimated in the inner region, while overestimated in the outskirts. The best-constrained and true profiles cross at approximately the half-mass radius of tracer satellites, as marked by the vertical red dashed line, leading to a good constraint on $M(<r_{half})$. There are about 11 ($\sim$39%) galaxy clusters in our analysis having their best-fitting inner and outer densities biasing from the truth in different directions while maintaining a good recovery of $M(<r_{half})$. Among them, seven have underestimated inner densities and overestimated outer densities, while four have overestimated inner densities and underestimated outer densities.

In previous studies, we have applied JAM to dwarf galaxies in numerical simulations to recover their dark matter distributions (Wang et al. 2022, 2023). We find that contraction or infalling motions can cause deviations from steady states. Such infalling motions reduce the velocity dispersions in inner regions, resulting in underestimated inner densities, and to maintain a good constraint on $M(<r_{half})$, the outer densities are overestimated. On the other hand, global expansion motions such as gas outflows can cause overestimated inner densities and underestimated outer densities.

Moreover, we have discussed in another study (Li et al. 2022) that galaxy cluster systems having overestimated $M(<r_{half})$ often have large virial ratios.[13] Clusters with the highest virial ratio values are usually unrelaxed systems with high kinetic energy, which may be caused by major mergers or active mass accretion, and thus the kinetic energy is increased within a short time. Li et al. (2022) showed a tight correlation between the bias in $M(<r_{half})$ and the system virial ratios.

In our current study, we have also investigated whether galaxy cluster systems with under/overestimated inner densities and over/underestimated outer densities have infalling/expansion motions in the tracer satellite population and in the gas and dark matter components. Unfortunately, we fail to see prominent correlations as in Wang et al. (2022). Moreover, we have looked at the correlation between the bias in $M(<r_{half})$ and the virial ratio and failed to see prominent correlations. We think this is mainly limited by our small number of tracer satellite galaxies and the associated large statistical errors. Note in our current analysis, the number of tracer satellites ranges from 70 to slightly more than 350, whereas Wang et al. (2022) used at least 6000 member star particles as tracers, and Li et al. (2022) in fact adopted dark matter particles in their simulations as tracers, instead of satellites or subhalos. The average number of tracers in galaxy clusters used by Li et al. (2022) is on the order of 10^5.

We note that the contraction/infalling or expansion/outflow motions are not the only ways of causing the systems to deviate from steady states. The deviation from steady states can be

---

[13] The virial ratio is defined as twice kinematical energy versus the potential energy of the system, calculated using all bound particles.
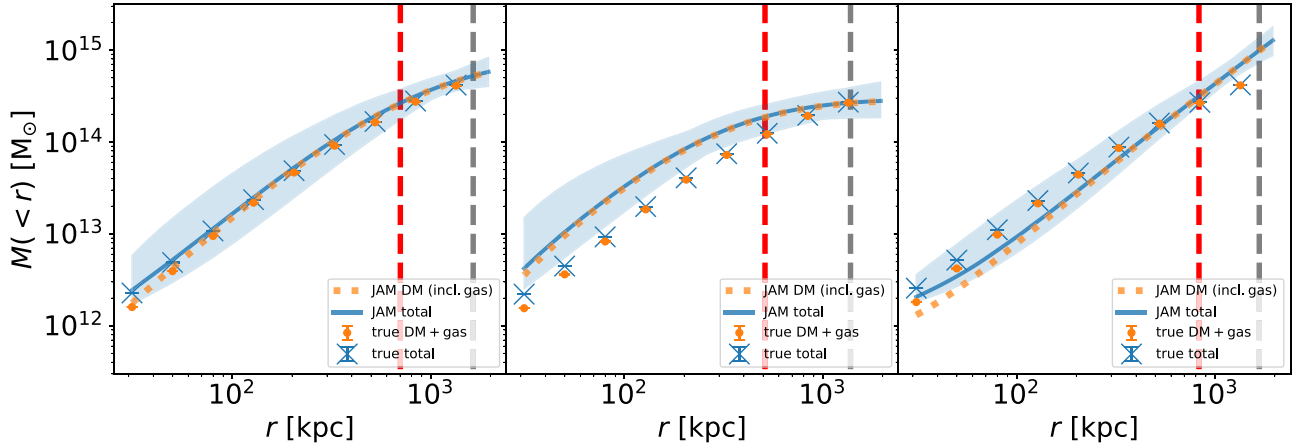
Figure 5. Comparison between the real and JAM-predicted density profiles for three example galaxy clusters from TNG300 and the three examples are shown in three different panels. The density profiles are calculated in three dimensions, and r in the x-axis label is the radius from the cluster center in three dimensions. The true total density profile is represented by blue crosses with error bars (comparable to the symbol size), and the blue solid curve is the JAM prediction. The blue-shaded region corresponds to the 1σ error by JAM. The true dark matter + gas density profiles are shown by orange dots, while the corresponding JAM predictions are shown by the orange dotted curves. Note JAM does not model the gas component separately, which is largely modeled within the dark matter component, so for fair comparisons, the orange dots correspond to the actual dark matter + gas density profiles in the simulation. The true total mass density profile corresponds to everything in the simulation, including stellar, dark matter, and gas, whereas the JAM-predicted total profile is the summation of the best-constrained dark matter and stellar components, with the stellar component directly inferred by deprojecting the stellar surface density distribution. Error bars of the true density profiles are calculated from the 1σ scatters of 100 bootstrap subsamples of particles in the galaxy clusters. The red and gray dashed vertical lines mark the half-mass radii of the tracer satellites and R_{200}.

caused by many other factors, such as the existence of massive and dynamically cold streams post-major mergers, the perturbation by a massive companion satellite galaxy, and the time evolution of the underlying gravitational potential. For the case shown in the middle panel of Figure 5, we discovered a massive companion located behind the cluster along the line of sight but passed our selection criterion along the line-of-sight direction. This is likely the reason causing the overestimate in $M(<r_{\rm half})$ for this system. For the other three systems having overestimated $M(<r_{\rm half})$, we have identified one system having a massive companion projected just beyond 2 Mpc, but we fail to see the similar existence of massive companions for the other two. However, we have tested our results by varying the magnitude gap when selecting our galaxy cluster systems. We find that a smaller magnitude gap in the selection, which means the possible existence of more massive companions, would end up with more cases corresponding to the middle panel of Figure 5.

Moreover, JAM assumes axisymmetry, whereas realistic galaxy cluster systems from TNG300 are not ideally axisymmetric. The deviation from the axisymmetric assumption is also responsible for the biases in the mass profiles. We find that different choices of line-of-sight direction with respect to the minor axis of our cluster systems can lead to different results for individual systems. For one system belonging to the classification in the middle panel of Figure 5, its major axis is more aligned with the line of sight, which is likely the cause for overestimated masses at most of the radii.

So far we have demonstrated a few typical cases of how the best-fitting density profiles deviate from the truth. However, what we directly fit are the velocity moments, instead of the density profiles. We thus show in Figure 6 the true (symbols) and best-fitting (lines) velocity dispersion profiles in projected radial bins along the major (green) and minor (black) axes of three galaxy clusters, which correspond exactly to the three systems we show in Figure 5.

In all three panels, the best-fitting models agree with the truth reasonably. However, the true velocity dispersion profiles

are not perfectly axisymmetric, with prominent differences between the left- and right-hand sides. However, JAM is an axisymmetric model. As a result, some of the asymmetric features are not possible to be ideally fit. For example, if looking at the velocity dispersion profiles in the left panel, the model tends to be higher than the actual velocity dispersions on the positive side of the x-axis and at large radii, and the difference is greater than the error bars, while the negative side is a better fit. We do not expect the axisymmetric JAM model to have an ideally good fit for this case.

4.3. Constraints on the Inclination Angle

Our analysis in the previous subsections is achieved by fixing the inclination angle, $incl$, to the angle between the line of sight and the minor axis calculated from the spatial distribution of tracer satellites in TNG300. In real observation, we do not know $incl$ in advance. Thus from now on, we treat $incl$ as a free parameter in our modeling. Figure 7 shows a comparison between the cases when $incl$ is fixed or set free. For most of the cases, fixing $incl$ or setting it free leads to differences in the best-constrained $M(<r_{\rm half})$ and M_{200} smaller than the error bars. With $incl$ as a free parameter, the biases in $M(<r_{\rm half})$ and M_{200} become -0.01 and 0.03 dex, and the scatters become 0.11 and 0.15 dex. The biases are not significantly different from the values when fixing $incl$ to the truth (-0.02 and 0.01 dex; see Section 4.1). The scatter in $M(<r_{\rm half})$ gets slightly larger, as compared to the value of 0.09 dex in $M(<r_{\rm half})$ of Section 4.1. The readers can also refer to the top and middle rows of Table 1 for a summary of these values.

Figure 8 shows the error contours for the same system as Figure 4. The constraint on $incl$ is not tight, with a 1σ uncertainty of about 30 deg. Most of the other parameters do not show strong correlations with $incl$, except for λ, which shows some positive correlations with $incl$. As a result, the best-constrained values of λ differ more significantly between Figures 4 and 8. The best constraints on the other model
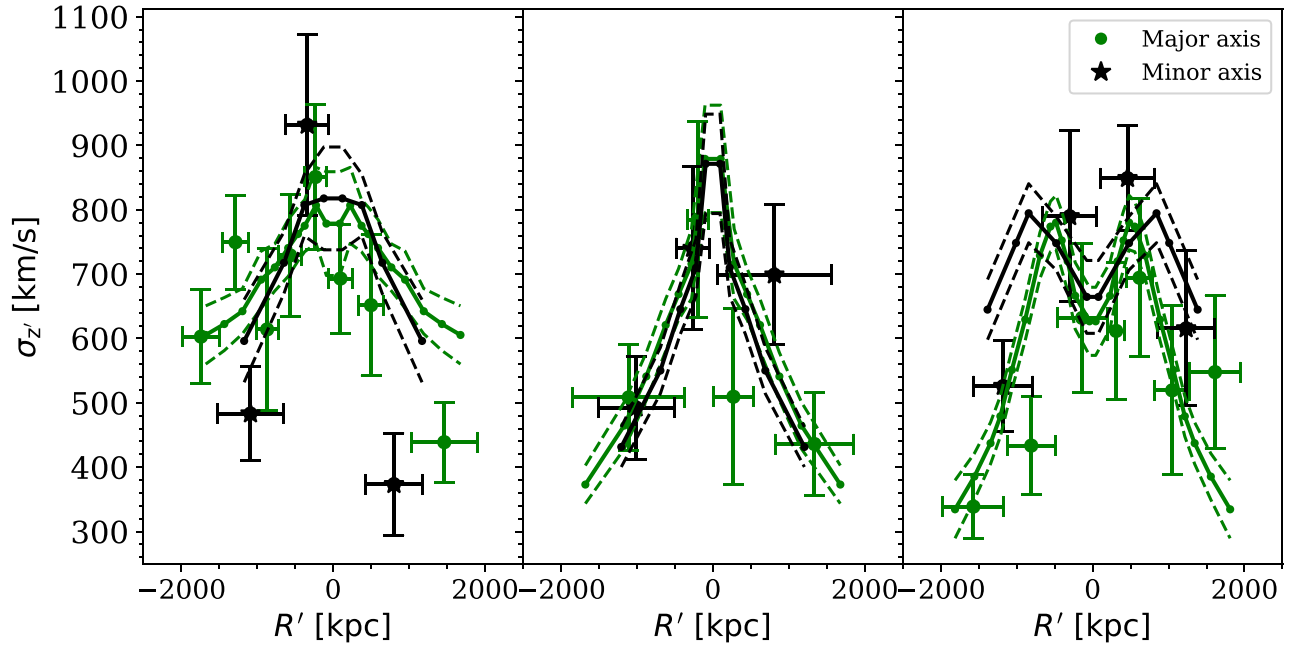
Figure 6. Line-of-sight (z' component) velocity dispersion profiles of member satellites in three galaxy clusters, binned within sectors of $\pm 45°$ to the major (green) and minor (black) axes of the cluster systems. Each bin contains 15 satellites. R' indicates the projected distances to the cluster center in the corresponding sectors along the major or minor axes in the image plane. The x and y errors indicate the bin width and the 1σ scatters, respectively. Green and black solid curves show the best model predictions along the major and minor axes. The three galaxy clusters correspond exactly to the three clusters shown in Figure 5.
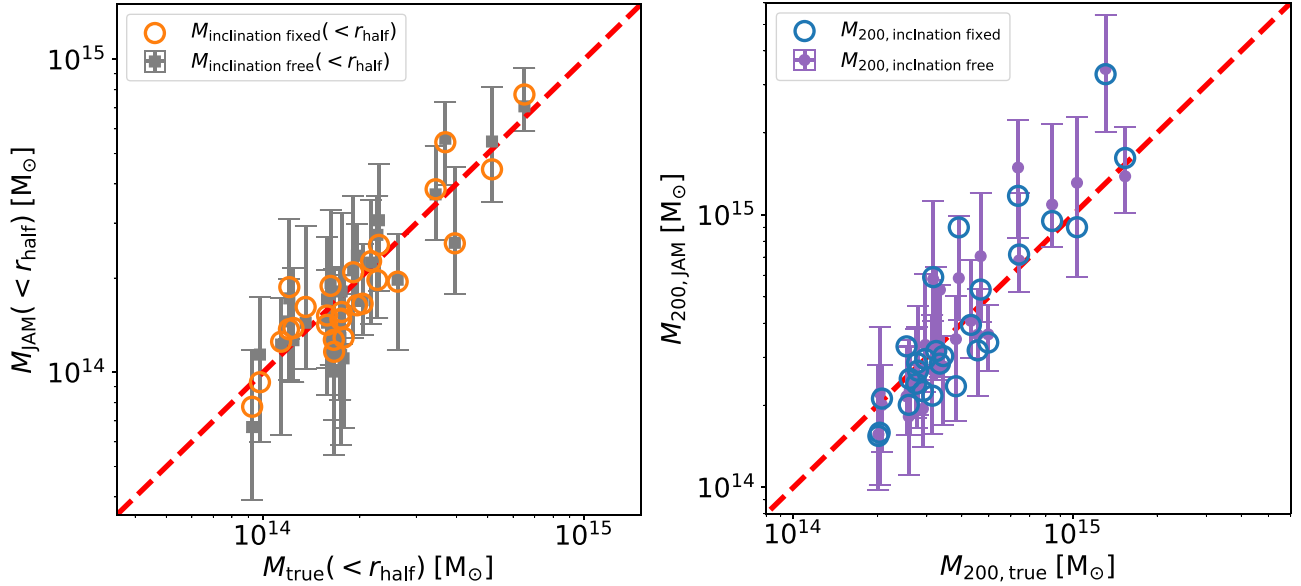
Figure 7. Left: best-fitting mass within the half-mass–radius of tracer satellites ($M(<r_{half})$) vs. truth for 28 galaxy clusters from TNG300. Here we set the inclination, *incl*, as a free model parameter, and the results are shown as gray squares with error bars. Empty orange circles are repeats of the measurements in the previous Figure 3 when *incl* is fixed to the truth in the simulation. Error bars for the red circles are comparable to those for the orange squares and are hence not repeatedly shown. Right: similar to the left panel, but for the virial mass (M_{200}). The blue circles are exactly the same as those in Figure 3.

parameters agree well within 1σ either fixing *incl* or setting *incl* free.

The frequencies corresponding to the cases in the three panels of Figure 5 remain largely similar when *incl* is a free parameter. So we do not repeatedly show the examples.

4.4. The Effect of Foreground and Background Contamination

The results presented so far are based on using bound satellites as tracers. However, in real observation, satellite galaxies are selected in the redshift space, which may suffer

from contamination by foreground and background galaxies (purity), and true satellite galaxies might be missing (completeness).

In order to better mimic the selection of satellite galaxies in real observations, we project the TNG300 simulation box along the Z-axis, i.e., the line of sight, also defined as the z'-axis in the observing frame. Tracer satellites are selected as those companions that are projected within 2 Mpc and with LOSV differences with respect to the central galaxy smaller than 2000 km s^{-1}. By selecting companion galaxies in this volume,
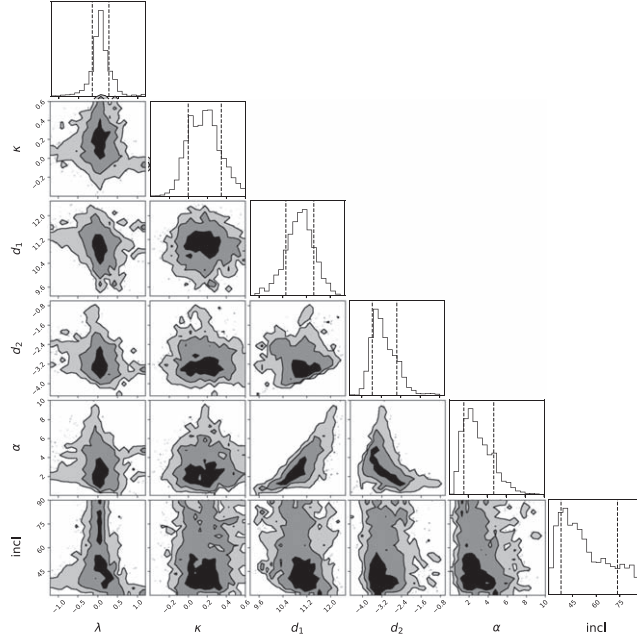
Figure 8. Similar to Figure 4, but now the inclination angle, *incl*, is treated as a free model parameter.
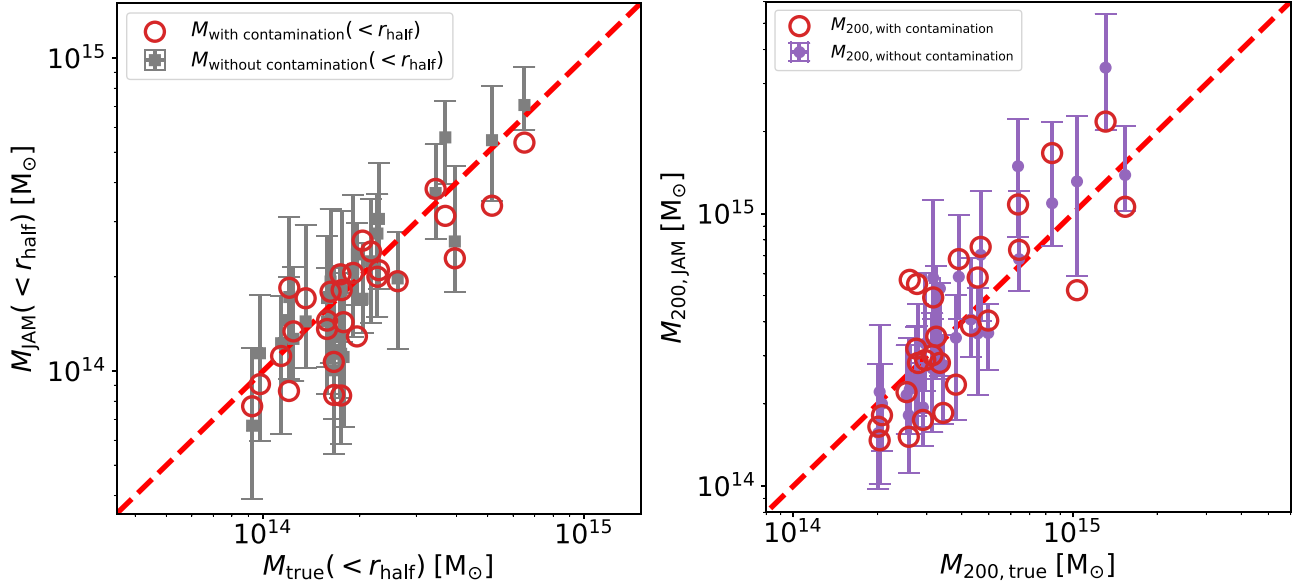
Figure 9. Left: best-fitting mass within the half-mass radius of tracer satellites ($M(<r_{half})$) vs. truth for 28 galaxy clusters from TNG300. Gray squares are exactly the same as those in Figure 8. After selecting tracer satellites according to the LOSV differences, we include ~10% contamination, and the corresponding results are shown as red empty circles. Error bars for the red circles are comparable to those for the orange squares and are hence not repeatedly shown. Right: similar to the left panel, but for the virial mass, M_{200}. The purple dots are exactly the same as those in Figure 3. The inclination angle, *incl*, is set as a free model parameter for results in both panels. We do not see prominent differences between the results before and after including contaminations.

we find on average 88% of true satellite galaxies in the simulation can be included, while there is only ~11% contamination by unbound galaxies. Note for results in this subsection, we treat *incl* as a free parameter.

Figure 9 shows a comparison of the best-recovered masses, based on true bound satellite galaxies and based on companions selected in projection as described above. Perhaps because of the reason that the fraction of contamination is as low as ~11%, the results before and after considering the contamination do not show significant differences for most systems. The

associated biases and scatters for $M(<r_{half})$ and M_{200} are shown in the bottom row of Table 1. Compared with the middle row when only bound satellites are used (no contamination), the biases and scatters only become slightly larger.

Our results in Figure 9 suggest that with the selection of companions projected in 2 Mpc and within 2000 km s^{-1} along the line of sight, the contamination of fore/background can be controlled to be as low as 11%, and the dynamical modeling outcome has slightly larger biases and scatters than using true bound satellites as tracers.
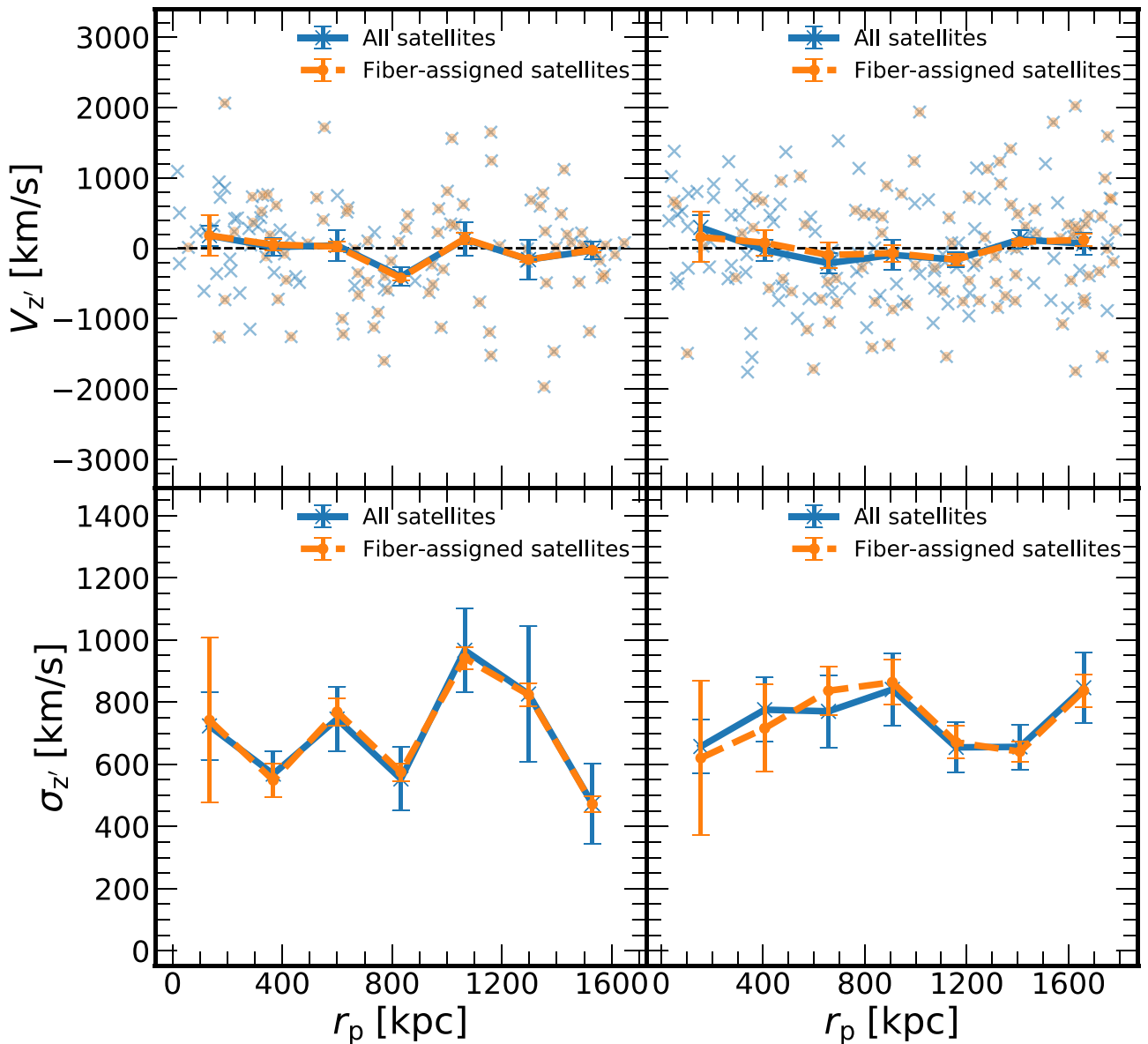
Figure 10. Top: LOSV profiles based on satellites of two randomly selected galaxy clusters from the mock DESI BGS catalog, denoted as Cluster1 and Cluster2. The mean velocities are binned and calculated in projected circular annuli, and we use r_p to denote the projected distance to the cluster center. The blue solid curves represent the mean velocity profiles based on the full set of bound companion satellites, and the orange dashed curves show the mean velocity profiles based on a subset of satellites with successful spectroscopic redshift measurements after incorporating fiber assignment and the redshift success rate in the mock. The blue crosses and orange dots correspond to individual satellites before and after accounting for fiber assignment. The profiles are derived from the mean of 32 times different fiber assignment tests and the error bars represent the 1σ scatters. The errors of the blue solid curves are based on the 1σ scatters of 100 bootstrap subsamples, while they are calculated as the 1σ scatters of the 32 different fiber assignment tests for the orange dashed curves. Bottom: curves similar to the top panels, but showing the LOSV dispersion profiles for Cluster1 and Cluster2. All panels are based on the flux limit of $r < 19.5$.

4.5. Fiber Incompleteness and the Dependence on Flux Limit

In addition to the projection effects and the contamination by foreground or background galaxies, real spectroscopic observations also suffer from fiber incompleteness and failures in redshift measurements; hence not all photometrically observed satellites would have spectroscopically measured LOSVs. The so-called fiber collision effect, in which two fibers cannot be placed closer than a certain angular separation, is more severe in dense cluster regions. As having been evaluated by Smith et al. (2019), with the DESI Bright Galaxy Survey fiber assignment strategy, the completeness fraction may be as low as 20% for the worst cases in dense cluster regions. It is thus important to consider the effect of fiber incompleteness.

In JAM, the possible effects of fiber incompleteness come from two aspects: (1) the projected number density profile of tracer satellites is modified; (2) fiber incompleteness may change the velocity and velocity dispersion profiles. For (1), if one knows about the exact completeness fraction as a function of the projected distance to the cluster center (selection effect), corrections can in principle be made. For (2), the essential point is whether the subsample of satellites that have successful spectroscopic redshift measurements would alter the velocity and velocity dispersion profiles, compared with the full set of companion satellites.

In order to check point (2) above, we look into a mock DESI BGS catalog based on the MXXL simulation (Smith et al. 2017). The readers can check Section 2.3 for details. Using the
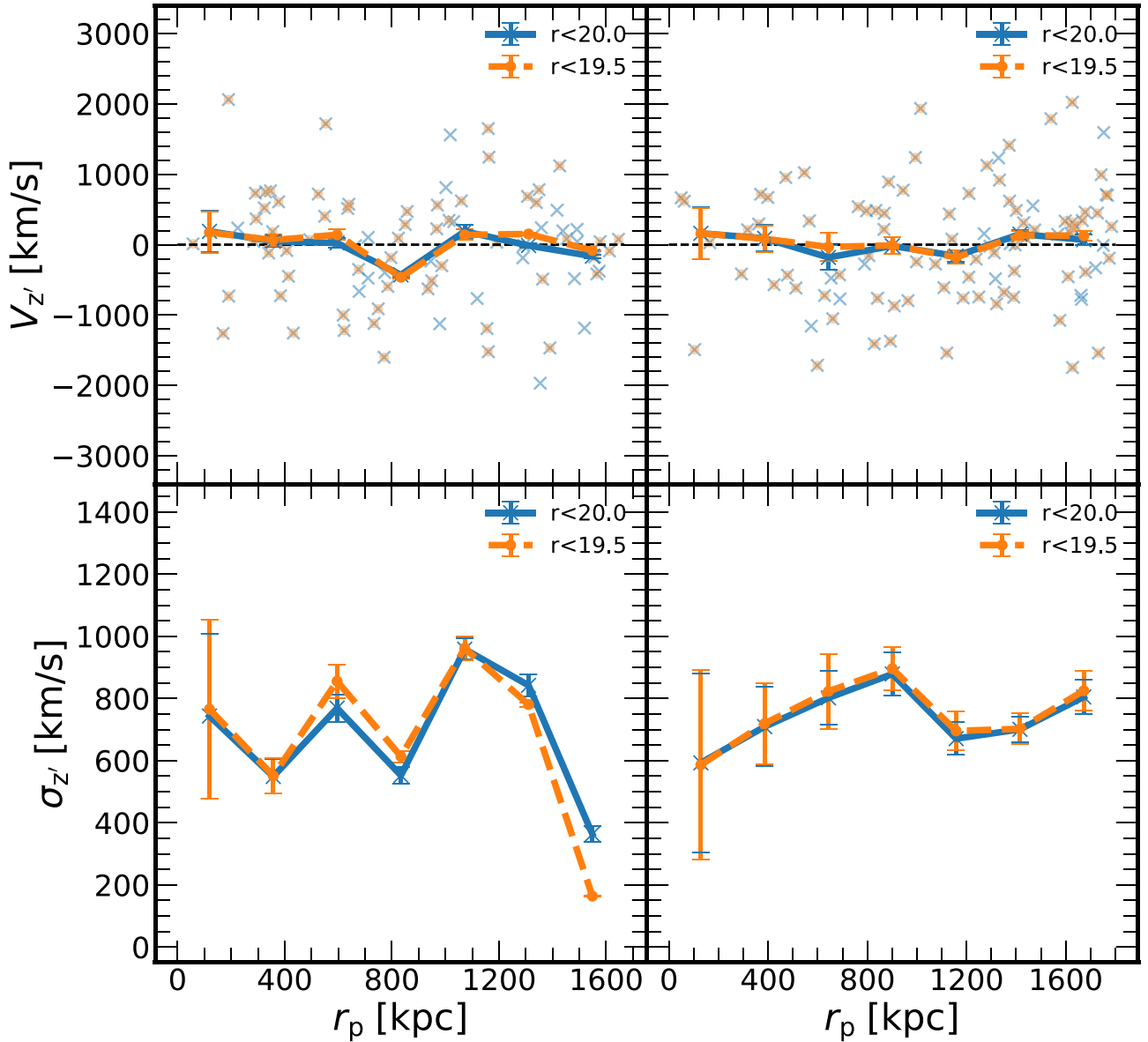
Figure 11. Similar to Figure 10, but now we compare the velocity (upper panels) and velocity dispersion (lower panels) profiles for two different flux limits (r-band flux limit of $r < 20.0$ and $r < 19.5$, in blue and orange as shown by the legend). The mean velocities and velocity dispersions are binned and calculated in projected circular annuli, and we use r_p to denote the projected distance to the cluster center All curves in all panels are based on the fiber-assigned satellite galaxies. The profiles are derived from the mean of 32 times different fiber assignment tests and the error bars represent the 1σ scatters of these tests.

mock catalog, we investigate whether the velocity dispersion profiles are changed before and after considering the effect of fiber incompleteness.

Figure 10 shows the LOSVs and velocity dispersions as a function of the projected distance, r_p, to the cluster center, for two example galaxy clusters. We compare the velocity and velocity dispersion profiles before and after considering the effect of fiber incompleteness. The profiles are derived from the mean of 32 different random realizations of the fiber assignment algorithm, and the error bars represent the 1σ scatters. The differences between the blue and orange curves are very small at all radii. Compared with the errors, we do not see any significant differences between the velocity dispersion profiles before and after incorporating the fiber incompleteness, indicating fiber incompleteness in DESI is unlikely to modify the velocity dispersions of observed satellite galaxies compared

with the full sample of satellites; hence the dynamical modeling results are not likely to be affected either.

In addition to the effect of fiber incompleteness, we also examine the impact of flux limit on our analysis. The DESI BGS mock catalog includes 84 galaxy cluster systems within the DESI Year 5 footprint with a halo mass range of $14.3 < \log_{10} M_{\rm halo}/M_\odot < 15$ at $z < 0.2$, that can have more than 100 satellites brighter than $r = 19.5$ assigned with fibers. $r < 19.5$ is the flux limit for the DESI BGS bright sample. The flux limit for the less complete BGS faint sample is $r < 20.175$. Since the flux limit of the current version of the DESI BGS mock we are using is $r < 20$ and if the flux limit is adjusted to $r < 20$, there would be 165 galaxy clusters that can have more than 100 satellites above the flux limit. We perform tests to assess whether the exclusion of faint objects would affect the velocity and velocity dispersion profiles.

In Figure 11, we present the radial velocity and velocity dispersion profiles for two representative clusters, subject to different flux limit cuts of their satellites ($r < 19.5$ and $r < 20.0$). The upper panels show the velocity profiles, where the blue and orange curves correspond to the flux limits of $r < 20.0$ and $r < 19.5$, respectively. We can see the orange curves are within the error bars of the blue curves. The blue crosses and orange dots behind the curves represent the velocities of individual satellites with $r < 20.0$ and $r < 19.5$, respectively. The $V_{z'} = 0$ line goes well through both symbols, based on which we do not see significant selection biases. The lower panels show the velocity dispersion profiles. It can be seen that the orange curves are closely aligned with the blue curves. The results are thus unlikely to be significantly affected by the different choices of flux limits in DESI.

Our results indicate that the velocity and velocity dispersion profiles are not sensitive to the choice of flux limit in the DESI survey. Note as we have mentioned in Section 2.3, the mock DESI BGS catalog we are using is by Smith et al. (2017). The fiber assignment algorithm, the flux limit for the BGS faint sample, and the number of passes are currently being updated for the latest version of the DESI BGS mock. These updates are not yet fully fixed, so we are focusing on the DESI BGS mock by Smith et al. (2017). However, we expect these changes will not have a significant impact on the results presented in our analysis.

5. Conclusions

In this study, we investigate the performance of the JAM method, when it is applied to satellite galaxies in galaxy clusters to recover the underlying matter distribution. Twenty-eight galaxy cluster systems are selected from the cosmological and hydrodynamical TNG300-1 simulation (TNG300 in short), with a halo mass of $\log_{10} M_{200}/M_\odot > 14.3$.

The best-constrained total matter density profiles by JAM deviate from the truth in different ways. We divide the deviations into three different categories: (1) very good overall agreement with the true density profiles at all radii (29%), with the deviations smaller than the errors of the true profiles; (2) over/underestimates at most radii (32%) and (3) under/overestimates within the half-mass radius of tracer satellites (r_{half}) and over/underestimates outside r_{half}, which maintains a good prediction of $M(<r_{half})$ (39%). Most of the best-constrained models are still consistent with the true profiles within 1σ statistical uncertainties of the model.

If only using true bound satellites as tracers and fixing the inclination parameter to the angle between the line of sight and the minor axis of satellite spatial distributions, the best-constrained total mass within the half-mass radius of satellites, $M(<r_{half})$, and the virial mass, M_{200}, have average biases of -0.02 and 0.01 dex, with average scatters of 0.09 dex and 0.15 dex. If treating the inclination as a free model parameter, the biases become -0.01 and 0.03 dex for $M(<r_{half})$ and M_{200}, with mean scatters of 0.11 and 0.15 dex. The constraint on $M(<r_{half})$ is tighter than that of M_{200}.

If selecting tracer companions in the redshift space, by requiring that their LOSV differences are within ± 2000 km s^{-1} to the cluster central galaxy, we can maintain a high completeness of 88%, with the fraction of contamination by foreground and background galaxies as 11%. The average biases are then -0.06 dex for $M(<r_{half})$ and 0.01 dex for M_{200}, with mean scatters of 0.12 and 0.18 dex.

We look into a mock DESI BGS light-cone catalog and find within the DESI Year 5 footprint, 84 galaxy cluster systems at redshift $z < 0.2$ can have more than 100 satellite galaxies brighter than $r = 19.5$ and with fiber assignments. If the flux limit is changed to $r < 20$, there are 165 galaxy clusters that satisfy the selection. Hence it is promising to constrain the mass of galaxy clusters using satellite dynamics with future DESI data. Based on the mock DESI catalog, we test the effect of fiber incompleteness and the dependence on the survey flux limit and see no significant changes in the velocity and velocity dispersion profiles within R_{200}. Thus selection effects brought in by fiber assignments and survey flux limits are unlikely to affect the dynamical modeling outcomes.

We conclude it is promising to apply JAM to satellite galaxies in galaxy clusters in ongoing and future deep spectroscopic surveys, to constrain the underlying density profiles and total mass of individual cluster systems. Our quoted amounts of biases and scatters can be used as corrections to future observational constraints.

ORCID iDs

Rui Shi https://orcid.org/0000-0001-7404-3706
Wenting Wang https://orcid.org/0000-0002-5762-7571
Zhaozhou Li https://orcid.org/0000-0001-7890-4964

Ling Zhu ⓘ https://orcid.org/0000-0002-8005-0870
Alexander Smith ⓘ https://orcid.org/0000-0002-3712-6892
Shaun Cole ⓘ https://orcid.org/0000-0002-5954-7903
Qingyang Li ⓘ https://orcid.org/0000-0003-0771-1350
Jiaxin Han ⓘ https://orcid.org/0000-0002-8010-6715

References

Abazajian, K. N., Adelman-McCarthy, J. K., Agüeros, M. A., et al. 2009, ApJS, 182, 543

Anderson, M. E., Gaspari, M., White, S. D. M., Wang, W., & Dai, X. 2015, MNRAS, 449, 3806

Angulo, R. E., Springel, V., White, S. D. M., et al. 2012, MNRAS, 426, 2046

Arnaud, M., Pratt, G. W., Piffaretti, R., et al. 2010, A&A, 517, A92

Biviano, A., Murante, G., Borgani, S., et al. 2006, A&A, 456, 23

Boselli, A., Roehlly, Y., Fossati, M., et al. 2016, A&A, 596, A11

Cappellari, M. 2008, MNRAS, 390, 71

Conroy, C. 2013, ARA&A, 51, 393

Davis, M., Efstathiou, G., Frenk, C. S., & White, S. D. M. 1985, ApJ, 292, 371

De Graaff, A., Cai, Y.-C., Heymans, C., & Peacock, J. A. 2019, A&A, 624, A48

DESI Collaboration, Aghamousa, A., Aguilar, J., et al. 2016, arXiv:1611.00036

Diaferio, A. 1999, MNRAS, 309, 610

Diaferio, A., & Geller, M. J. 1997, ApJ, 481, 633

Doe, S., Nguyen, D., Stawarz, C., et al. 2007, in ASP Conf. Ser. 376, Astronomical Data Analysis Software and Systems XVI, ed. R. A. Shaw, F. Hill, & D. J. Bell (San Francisco, CA: ASP), 543

Driver, S. P., Hill, D. T., Kelvin, L. S., et al. 2011, MNRAS, 413, 971

Driver, S. P., Norberg, P., Baldry, I. K., et al. 2009, A&G, 50, 5.12

D'Souza, R., & Rix, H.-W. 2013, MNRAS, 429, 1887

Emsellem, E., Monnet, G., & Bacon, R. 1994, A&A, 285, 723

Foëx, G., Böhringer, H., & Chon, G. 2017, A&A, 606, A122

Fong, M., & Han, J. 2021, MNRAS, 503, 4250

Fong, M., Han, J., Zhang, J., et al. 2022, MNRAS, 513, 4754

Foreman-Mackey, D., Hogg, D. W., Lang, D., & Goodman, J. 2013, PASP, 125, 306

Freeman, P., Doe, S., & Siemiginowska, A. 2001, Proc. SPIE, 4477, 76

Gao, H., Han, J., Fong, M., Jing, Y. P., & Li, Z. 2023, ApJ, 953, 37

Gifford, D., Miller, C., & Kern, N. 2013, ApJ, 773, 116

González-Samaniego, A., Bullock, J. S., Boylan-Kolchin, M., et al. 2017, MNRAS, 472, 4786

Hahn, C., Wilson, M. J., Ruiz-Macias, O., et al. 2023, AJ, 165, 253

Han, J., Eke, V. R., Frenk, C. S., et al. 2015, MNRAS, 446, 1356

Han, J., Wang, W., Cole, S., & Frenk, C. S. 2016, MNRAS, 456, 1003

Harris, C. R., Millman, K. J., van der Walt, S. J., et al. 2020, Natur, 585, 357

Hernández-Monteagudo, C., Ma, Y.-Z., Kitaura, F. S., et al. 2015, PhRvL, 115, 191301

Huang, S., Leauthaud, A., Greene, J. E., et al. 2018, MNRAS, 475, 3348

Hunter, J. D. 2007, CSE, 9, 90

Kimm, T., Somerville, R. S., Yi, S. K., et al. 2009, MNRAS, 394, 1131

Kodi Ramanah, D., Wojtak, R., & Arendse, N. 2021, MNRAS, 501, 4080

Kollmeier, J. A., Zasowski, G., Rix, H.-W., et al. 2017, arXiv:1711.03234

Li, C., Jing, Y. P., Mao, S., et al. 2012, ApJ, 758, 50

Li, C., Zhu, L., Long, R. J., et al. 2020, MNRAS, 492, 2775

Li, Q., Han, J., Wang, W., et al. 2021, MNRAS, 505, 3907

Li, Q., Han, J., Wang, W., et al. 2022, MNRAS, 514, 5890

Lim, S. H., Mo, H. J., Li, R., et al. 2018, ApJ, 854, 181

Lim, S. H., Mo, H. J., Wang, H., & Yang, X. 2020, ApJ, 889, 48

Mamon, G. A., Biviano, A., & Boué, G. 2013, MNRAS, 429, 3079

Marinacci, F., Vogelsberger, M., Pakmor, R., et al. 2018, MNRAS, 480, 5113

Merson, A. I., Baugh, C. M., Helly, J. C., et al. 2013, MNRAS, 429, 556

More, S., van den Bosch, F. C., & Cacciato, M. 2009a, MNRAS, 392, 917

More, S., van den Bosch, F. C., Cacciato, M., et al. 2009b, MNRAS, 392, 801

More, S., van den Bosch, F. C., Cacciato, M., et al. 2011, MNRAS, 410, 210

Myers, A. D., Moustakas, J., Bailey, S., et al. 2023, AJ, 165, 50

Naiman, J. P., Pillepich, A., Springel, V., et al. 2018, MNRAS, 477, 1206

Navarro, J. F., Frenk, C. S., & White, S. D. M. 1996, ApJ, 462, 563

Navarro, J. F., Frenk, C. S., & White, S. D. M. 1997, ApJ, 490, 493

Nelson, D., Pillepich, A., Springel, V., et al. 2018, MNRAS, 475, 624

Nelson, D., Springel, V., Pillepich, A., et al. 2019, ComAC, 6, 2

Old, L., Skibba, R. A., Pearce, F. R., et al. 2014, MNRAS, 441, 1513

Pérez, F., & Granger, B. E. 2007, CSE, 9, 21

Pillepich, A., Springel, V., Nelson, D., et al. 2018, MNRAS, 473, 4077

Pintos-Castro, I., Yee, H. K. C., Muzzin, A., Old, L., & Wilson, G. 2019, ApJ, 876, 40

Planck Collaboration, Ade, P. A. R., Aghanim, N., et al. 2013, A&A, 557, A52

Planck Collaboration, Ade, P. A. R., Aghanim, N., et al. 2016, A&A, 594, A13

Rasia, E., Meneghetti, M., Martino, R., et al. 2012, NJPh, 14, 055018

Rykoff, E. S., Rozo, E., Busha, M. T., et al. 2014, ApJ, 785, 104

Sales, L. V., Navarro, J. F., Abadi, M. G., & Steinmetz, M. 2007, MNRAS, 379, 1464

Schlegel, D. J., Kollmeier, J. A., Aldering, G., et al. 2022, arXiv:2209.04322

Smith, A., Cole, S., Baugh, C., et al. 2017, MNRAS, 470, 4646

Smith, A., He, J.-h., Cole, S., et al. 2019, MNRAS, 484, 1285

Springel, V. 2010, MNRAS, 401, 791

Springel, V., Pakmor, R., Pillepich, A., et al. 2018, MNRAS, 475, 676

Springel, V., White, S. D. M., Tormen, G., & Kauffmann, G. 2001, MNRAS, 328, 726

Sun, Z., Yao, J., Dong, F., et al. 2022, MNRAS, 511, 3548

Takada, M., Ellis, R. S., Chiba, M., et al. 2014, PASJ, 66, R1

van den Bosch, F. C., Lange, J. U., & Zentner, A. R. 2019, MNRAS, 488, 4984

Virtanen, P., Gommers, R., Oliphant, T. E., et al. 2020, NatMe, 17, 261

Wagoner, E. L., Rozo, E., Aung, H., & Nagai, D. 2021, MNRAS, 504, 1619

Walker, M. G., & Peñarrubia, J. 2011, ApJ, 742, 20

Wang, H., Mo, H. J., Chen, S., et al. 2018, ApJ, 852, 31

Wang, W., Han, J., Cautun, M., Li, Z., & Ishigaki, M. N. 2020, SCPMA, 63, 109801

Wang, W., Han, J., Cooper, A. P., et al. 2015, MNRAS, 453, 377

Wang, W., Han, J., Sonnenfeld, A., et al. 2019, MNRAS, 487, 1580

Wang, W., White, S. D. M., Mandelbaum, R., et al. 2016, MNRAS, 456, 2301

Wang, W., Zhu, L., Jing, Y., et al. 2023, ApJ, 956, 91

Wang, W., Zhu, L., Li, Z., et al. 2022, ApJ, 941, 108

Watkins, L. L., van de Ven, G., den Brok, M., & van den Bosch, R. C. E. 2013, MNRAS, 436, 2598

Wetzel, A. R., Tinker, J. L., Conroy, C., & van den Bosch, F. C. 2013, MNRAS, 432, 336

Wolf, J., Martinez, G. D., Bullock, J. S., et al. 2010, MNRAS, 406, 1220

Yang, X., Mo, H. J., van den Bosch, F. C., et al. 2007, ApJ, 671, 153

Yang, X., Xu, H., He, M., et al. 2021, ApJ, 909, 143

Zhu, L., Romanowsky, A. J., van de Ven, G., et al. 2016, MNRAS, 462, 4001